# Direct mapping of local director field of nematic liquid crystals at the nanoscale

Yu Xia[a], Francesca Serra[a,b,c], Randall D. Kamien[b], Kathleen J. Stebe[c], and Shu Yang[a,1]

[a]Department of Materials Science and Engineering, University of Pennsylvania, Philadelphia, PA 19104; [b]Department of Physics and Astronomy, University of Pennsylvania, Philadelphia, PA 19104; and [c]Department of Chemical and Biomolecular Engineering, University of Pennsylvania, Philadelphia, PA 19104

Liquid crystals (LCs), owing to their anisotropy in molecular ordering, are of wide interest in both the display industry and soft matter as a route to more sophisticated optical objects, to direct phase separation, and to facilitate colloidal assemblies. However, it remains challenging to directly probe the molecular-scale organization of nonglassy nematic LC molecules without altering the LC directors. We design and synthesize a new type of nematic liquid crystal monomer (LCM) system with strong dipole–dipole interactions, resulting in a stable nematic phase and strong homeotropic anchoring on silica surfaces. Upon photopolymerization, the director field can be faithfully "locked," allowing for direct visualization of the LC director field and defect structures by scanning electron microscopy (SEM) in real space with 100-nm resolution. Using this technique, we study the nematic textures in more complex LC/colloidal systems and calculate the extrapolation length of the LCM.

nematic liquid crystal polymers | dipole–dipole interactions | topological defects | photo-cross-linking | nanoscale imaging

Ubiquitous as they are, it sometimes escapes our attention that liquid crystals (LCs) are the original nanomaterial. The manipulation of these nanometer-size molecules into coherent, centimeter-scale structures is now routine. Although we have become adept at deducing textures indirectly through optical microscopies (1–5), probing the molecular-scale organization requires either a glassy material or rapid cooling of samples, providing metastable states that can be directly visualized through scanning electron microscopy (SEM), transmission electron microscopy (TEM), and atomic force microscopy (AFM) (6–8). Although these techniques are effective to study a variety of more complex LC phases, including smectic LCs (6, 7, 9), cholesteric and blue phases (10), and biological LC polymers (11, 12), nonglassy, low molecular weight nematic LCs (NLCs) reorient during fast freezing. Polymer nematics can be quenched into metastable states but organization of static configurations through surface alignment is difficult. Flow alignment can be used but that often precludes complex, molecular scale patterning of the boundary conditions, essential for controlling and manipulating topological defects (13, 14). Although an undesired nuisance in NLC displays, topological defects mediate many of the rich interactions between colloids in NLCs (15). The defects, bearing quantized topological charge, resemble the defects in superconductors (16), soft ferromagnets (17), and even cosmic strings and monopoles (18). The fluidity of the phase and the weakly first-order nematic–isotropic phase transition allow for direct visualization of the creation/annihilation of defects via the Kibble–Zurek mechanism (19). Further, defects in a flat sheet of nematic gel or glass can be used to bend or twist local directors, inducing 3D shapes (20, 21). It is therefore critical to be able to characterize the defect structures at the nanoscale in a variety of settings. Here, we report the design and synthesis of a nematic liquid crystal monomer (LCM) system that has strong homeotropic anchoring on silica surfaces and does not reorient its director field during polymerization. Thus, the optical signatures remain unchanged in the liquid crystal polymers (LCPs), allowing for direct visualization of the defect structures by SEM in real space with 100-nm resolution. Using this technique, we study the

nematic textures in more complex LC/colloidal systems and estimate the ratio between elastic and anchoring constants, i.e., the extrapolation length, of LCMs in the nematic phase.

## Results and Discussion

Visualization of topological defects has been achieved by dispersing polymer fibers in prealigned, low molecular weight NLC (22, 23). However, the polymer fibers, fabricated in situ via polymerization of LCMs, often phase separate from the nematic host; thus maintaining the LC director field in a nonglassy nematic host for direct visualization is thwarted. Moreover, the fibers themselves can perturb the nematic phase, inducing artifacts and spurious defects. Of course, to visualize the native director field responding to geometric surface cues we must use molecules that can be aligned reliably at interfaces of different topology, topography, and surface chemistry. Typically, the alignment of LCMs is controlled via mechanical rubbing of a polymer layer, use of a photo-alignment layer (21), mechanical stretching, or application of magnetic fields (24–28). However, these techniques are limited in their spatial resolution, especially in comparison with the highly refined ability to impart chemical anchoring on boundaries with complex topography and topology at the micro- and nanoscales, and also require high uniformity across the large sample areas. Although functional LCMs have been used for decades in conjunction with LCPs as actuators and sensors (24–29), it remains challenging to achieve faithful anchoring control at the level of the old stalwart, 4-cyano-4′-pentylbiphenyl (5CB). Meanwhile, slow relaxation of the bulk director field will lead to spurious defects in LCMs (or polydomain configurations) as shown in *SI Appendix*, Fig. S1 from widely used LCMs in the

literature; this inherent obstacle becomes increasingly obvious under complex confinement.

To address this, we specially designed and synthesized a series of LCMs (LCM_X1, LCM_X2, and LCM_X3) (Figs. 1 and 2) with both strong surface anchoring and highly stable nematic phases. These LCMs suppress spurious defects, leaving only those required energetically and topologically. The monomers all have the same aromatic ester-based mesogenic group, both common and inexpensive to synthesize, with an *ortho*-substituted nitro group but different terminal groups, epoxy and alkene, both of which are readily photo-cross-linkable at ambient conditions via photoacids and "click" chemistry, respectively. We confirmed the chemical structures via $^{1}$H-NMR (*SI Appendix*, Fig. S2). Similar LCMs terminated with epoxy or alkene groups have been reported with nematic phases in the literature (30) although they typically have very high phase transition temperatures, making it difficult to maintain the director field during polymerization due to the relatively low viscosity of the LCMs in the nematic phase. In addition, their anchoring properties have not been well characterized.

We introduced a pendant nitro group on the aromatic ring because it has been suggested that (*i*) LCs with a nitro group at the *ortho* position to a linkage ester group typically form a nematic phase with a relatively low phase transition temperature (31) and, more importantly, (*ii*) the introduction of a polar (e.g., nitro) or polarizable group into the chemical structure often results in an increase of molecular polarity, affecting molecular packing and, in turn, the phase stability of LCs (31). In particular, aromatic ester-based mesogens could achieve a stable nematic phase through strong intermolecular dipole–dipole interactions between carbonyl groups of adjacent molecules, an effect that increases with the strength of the molecular interaction (32, 33). In our system, we expect strong dipole–dipole interactions between carbonyl groups (dipole moment $\mu = 2.4$D) (34) that are evenly distributed along the molecule and a more polar nitro group ($\mu = 4.01$D) (34) in the middle of the molecule. Because each nitro group bonds randomly to one of the four sites from the adjacent LC molecule, crystallization is suppressed, as seen in analogous systems (30, 33, 35), leading to a highly stable nematic phase (*SI Appendix*, Fig. S3 and Movie S1) with strong surface anchoring properties for all LCMs we synthesized (Fig. 3 *A–C* and *SI Appendix*, Fig. S4). Here, we focused our study on LCM_X1 both because it has a large nematic window (>100 K) with the nematic phase starting slightly above its glassy transition temperature (~10 °C) and because the terminal epoxy groups could be rapidly and locally cross-linked by photoacids without large volume change—effectively locking the orientational order of mesogens for later SEM imaging.

We used patterned substrates that were well characterized in our laboratories, including membranes with cylindrical pores, micropillar arrays, and square-shaped one-dimensional (1D) microchannels with strong homeotropic anchoring (details in
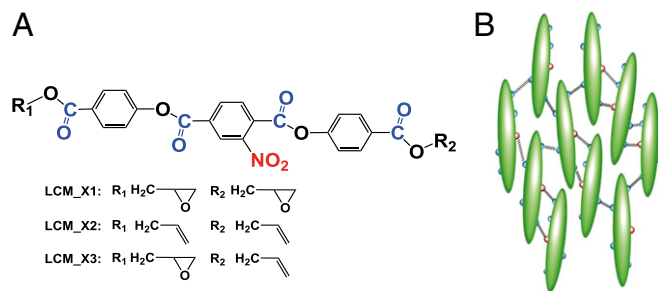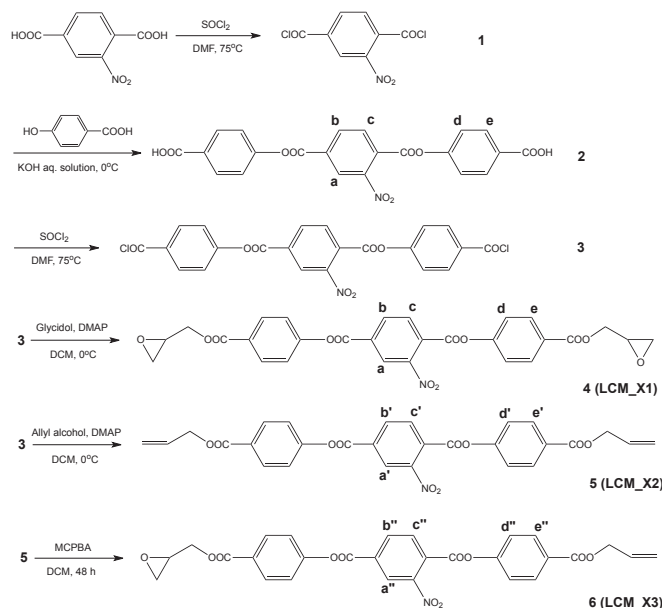


**Fig. 2.** Schematic illustrations of the synthesis of the nematic liquid crystal monomers. $^{1}$H-NMR spectra of protons labeled in each monomer can be found in *SI Appendix*, Fig. S2.

*Materials and Methods*) to study the alignment of newly synthesized LCMs in comparison with small molecule NLC, 5CB. As seen from the polarized optical microscopy (POM) and brightfield (BF) images shown in Fig. 3 *A–C*, both molecules are readily aligned with nearly identical director configurations on all patterned substrates despite the difference in surface treatments to align LCM_X1 vs. 5CB. For LCM_X1, homeotropic anchoring was achieved on silica-coated surfaces whereas planar anchoring was achieved on polyimide-treated surfaces (*SI Appendix*, Fig. S6). This is in sharp contrast to the behavior of commonly used LCMs, RM257 and LCM_AZO, which exhibit polydomains on the same substrates regardless of surface treatment (*SI Appendix*, Fig. S1). Note that the anchoring behavior of LCM_X1 shown in *SI Appendix*, Fig. S6 is visualized from SEM images of its LCP. As we discuss later, the LC director is maintained from LCM to LCP.

In cylindrical pores with homeotropic anchoring on all boundaries, the nematic director either forms a bulk point defect with integer topological charge (±1) in the center or "escapes into the third dimension" (36, 37) to separate two half-defects on the boundaries. Likewise, in the pillar arrays, there could be a bulk disclination ring surrounding the pillars (15) or an escape configuration where the defects are all concentrated next to the pillar edges. However, neither POM nor BF microscopy can distinguish these two modalities without further investigation of the director field through the whole sample or through the use of a variety of state-of-the-art tools such as confocal polarized microscopy.

To access the director information in these geometries, we cross-linked the LCMs through cationic polymerization of epoxy, a common reaction in negative-tone photoresists (38, 39). Compared with acrylate and methacrylate groups that are often used in radical polymerization of LCMs, epoxides have several advantages that are key to our LCM design: (*i*) They are insensitive to ambient oxygen. (*ii*) They can be cross-linked efficiently through chemically amplified ring-opening reactions; each photogenerated acid can initiate hundreds of reactions locally, rendering fast polymerization without large volume shrinkage seen in (meth)acrylate polymers. (*iii*) The bulky aromatic ester mesogens limit acid diffusion at room temperature; therefore,



**Fig. 1.** Schematic illustrations of (*A*) the chemical structures of various liquid crystal monomers, LCM_X1, LCM_X2, and LCM_X3 and (*B*) random intermolecular dipole–dipole interactions between nitro and carbonyl groups. Different colors represent different functional groups: red for nitro and blue for carbonyl.
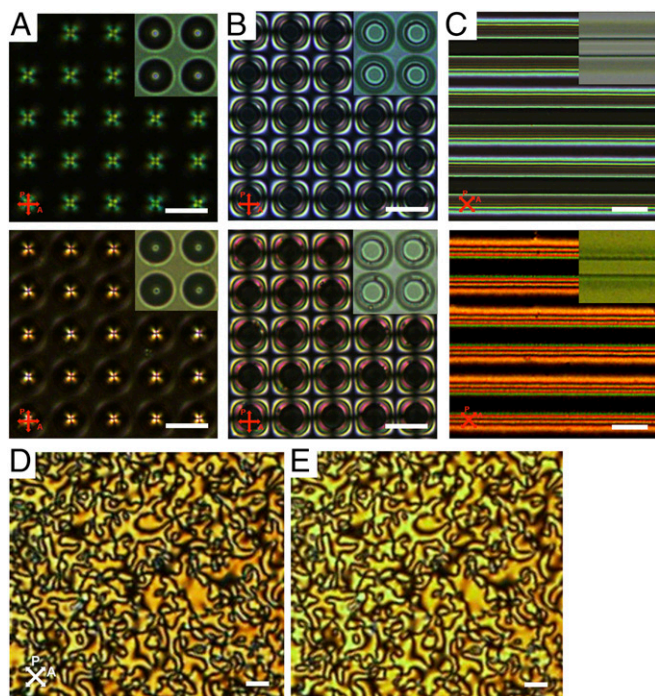
**Fig. 3.** POM and BF images of 5CB and LCM_X1. (*A–C*) POM and BF images of 5CB (*Top* panels) and LCM_X1 (*Bottom* panels) in (*A*) porous membranes (diameter, 10 μm; pitch, 15 μm; depth, 20 μm), (*B*) pillar arrays (diameter, 10 μm; pitch, 20 μm; height, 19 μm), and (*C*) square channels (width, 10 μm; pitch, 40 μm; depth, 20 μm) with homeotropic anchoring imposed at all surfaces. (*A*, *Insets*) BF image of LCs in pores where the dark dots at the center show possible defects; (*B*, *Insets*) BF image with black circles showing possible bulk line defects circumscribing the pillars; (*C*, *Insets*) BF image of a single ridge where the gray color indicates a distorted director field but no defect; (*D* and *E*) POM images of the schlieren texture of LCM_X1 before (*D*) and after (*E*) UV curing. The nearly identical nematic schlieren textures indicate that the LC director field is well maintained during polymerization. The slight change in color can be attributed to the difference in UV-vis absorption of monomer vs. polymer (*SI Appendix*, Fig. S5). After polymerization, the LCM-X1 appeared somewhat yellowish. (Scale bars, 20 μm.)

photopolymerization occurs locally. Together with the strong dipole–dipole intermolecular interactions, our LC molecules can lock in position effectively without altering the field direction during polymerization. Closely related are earlier studies of cationic photopolymerization of LC diepoxides (40, 41), which show that the NLC phase is maintained in the densely cross-linked network—in contrast to that from radical polymerization of diacrylates. It was noted, however, that unintentional heating by the high-intensity UV light could realign the mesogens, thus increasing the order parameter after curing (41). To prepare even cleaner data, we further suppressed reorientation during cross-linking by performing the UV curing at room temperature (~25 °C) with a low UV light intensity (2 mW/cm$^2$), keeping the viscous timescales longer than the polymerization timescale (details in *Materials and Methods*).

From the birefringence of the material (*Materials and Methods*) and the POM images of samples before and after polymerization (Fig. 3 *D* and *E* and *SI Appendix*, Fig. S7), we confirmed that on the micrometer scale the director field was preserved during polymerization. Once polymerized, we could use SEM to directly visualize the nematic texture with nanoscale resolution of the director configuration in various cross-sections obtained by fracturing the sample at room temperature. As shown in Fig. 4 *A–C* and *SI Appendix*, Figs. S6 and S8, the local director field is visible under SEM, represented by the

nanofiber-like fracture structures, the footprints of the director field. We note that the polymer itself does not form fibers. Rather, the oriented structures observed in SEM are a consequence of the anisotropic mechanical properties of LCPs, in which the bulk elastic modulus is usually much smaller perpendicular to the director (21, 42) and in which fractures occur along surfaces parallel to the director field (43, 44). The same type of fracture pattern can be observed in a nematic polymer that has some similarity with our LCPs (42). Following the fracture structures, we directly mapped the LC alignment with 100-nm resolution as illustrated by the red dotted line in Fig. 4 *A–C*. From Fig. 4*A* we determine the angle of molecular alignment at the surface to be 90° inside a wide channel; likewise, we can see that homeotropic anchoring breaks down when the director field is tightly confined as shown in Fig. 4 *B* and *C*. We can now directly visualize the defect structure in pores, pillar arrays, and 1D channels and observe that the director most often adopts an escaped configuration, avoiding defects in the bulk. By contrast, in POM the observed point- and line-like structures could just as well be the sign of a distorted director field or a defect. Further, from SEM images we can estimate the extrapolation length of the LCM (45) for planar and homeotropic anchoring (details in *SI Appendix*). We can estimate the elastic constant, which is on the order of a few pico-Newtons, in line with the elastic moduli of other LCs.

Armed with our careful study of the local director field of LCs on patterned surfaces, we turned to more complex director field structures: point defects and line defects created by colloids with homeotropic anchoring suspended in NLC. POM images in Fig. 5 depict typical pictures of hedgehog and Saturn ring defects surrounding silica colloids. Although numerous studies have focused on these defects in LC systems with varying colloidal size, geometry, and topology (46–49), direct visualization of the director structure is difficult, as is measuring the precise position of the induced topological defects. With fracture and SEM, here, we can determine these features with 100-nm accuracy. Consider, for example, the hedgehog in Fig. 5*A*; the defect can be seen as clearly located 2 μm above the colloid. In the same sample, we also found Saturn ring line defects around other silica colloids—Fig. 5*B* shows a typical defect with a slightly tilted director field. This slight tilting (tilting angle <15°) could not be detected by POM (Fig. 5*B*, *Inset*); however, it can be easily read from SEM.

We can use this technique to study the nematic textures in more complex LC systems. For instance, in Fig. 6 we show a LC cell treated for homeotropic alignment that we expect to image as black in POM. Instead, we see the appearance of blue regions, suggesting planar alignment, separated from the dark regions by disclination lines. Although such disclination lines are metastable in a neat NLC and relax very quickly, they can have a much longer lifetime when they are stabilized by colloids trapped at the disclinations. To observe the structures in Fig. 6 *B–E* with SEM, we again cooled down the sample and then cross-linked the LCM_X1. In Fig. 6*B* a disclination line generated at the boundary of the homeotropic and planar regions is shown. The disclination line can be identified by the fracture structure below and above the fracture plane in SEM as shown in Fig. 6*B* because of the different mechanical properties of the defect. Similar line defects can also be found in Fig. 6*C* and *SI Appendix*, Fig. S9, where silica colloids are trapped at the boundary. From the SEM images, we can observe the merging of the line defect in the bulk of LC and the Saturn ring surrounding the colloid. Further, it should be noted that bulk disclinations can also be stabilized by pinning to boundaries of the LC cell, as illustrated in Fig. 6*D*. The direct, clear visualization of the bending of the director field is useful to study the bending energy of LCs in various settings. Fig. 6*E* shows the LC orientation inside a planar-like region stabilized by silica colloids. The escaped configuration is surprising because it requires a large bending of the director field from the homeotropic boundaries to the center of
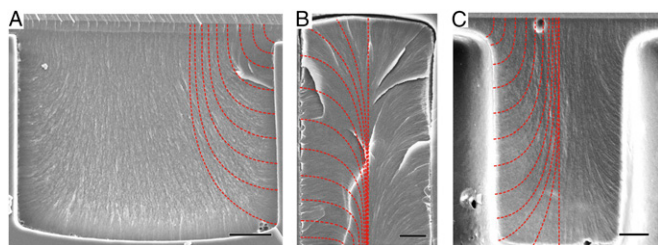
**Fig. 4.** (*A–C*) SEM images show the fracture structure of LCP after polymerization in a 1D microchannel (*A*), in a pore (*B*), and between two pillars (*C*). Escaping director field of LC can be observed from the orientation of the fracture structures in all three structures. The red dotted lines in *A–C* represent local director field of LCM mirrored in the other half of images. (Scale bars: *A*, 5 μm; *B* and *C*, 2 μm.)

the LC cell, resulting in a high elastic energy in the bulk of this 2D LC thin film (∼8 μm). A clarifying example of this behavior can be found in *SI Appendix*, where we show a SEM image of a small escape region whose boundaries could be both visualized in the same picture (*SI Appendix*, Fig. S10). The SEM images provide us a detailed director configuration in this small region, where the planar region starts at the surface of a colloid with an associated defect with charge −1, escapes in the direction determined by the defect structure around the colloid, and finally ends at another colloid surface. These SEM studies thus provide us the capability to fully explore LC anchoring behaviors inside LC cells featuring complex topology and also to "lock" and observe metastable states.

In conclusion, we designed and synthesized a new LCM system with strong dipole–dipole interactions, resulting in a stable nematic phase and precise control of molecular anchoring and alignment on different boundary conditions. The director field can be faithfully "locked" by photo-cross-linking, allowing for direct mapping of the LC director field and defect structures by SEM. In turn, we can calculate the extrapolation length and estimate the elastic and anchoring constants of LCs (see *SI Appendix* for detailed discussion and *SI Appendix*, Figs. S11 and S12). This molecular design strategy can be extended to other substituents (e.g., to induce hydrogen bonding) and bridging groups that connect the mesogen and epoxy group to fine-tune the mesomorphic properties. Moreover, our LC monomers are low cost; e.g., LCM_X1 can be produced at a cost of ∼10% that of 5CB, but with equal flexibility to be aligned on various boundary conditions. This newfound ability provides us with tools to enhance our understanding of anchoring, defects, and elasticity of short-molecule nematics, which will enable the further control of bulk structures via nanoscale patterning of the substrate and surface chemistry. We anticipate that by directly photopatterning a 2D sheet of NLC elastomer or glass with embedded defects and elasticity, followed by actuation by heat or light, we could induce folding into 3D.

## Materials and Methods

**Materials.** All chemicals were used without further purification. Dimethylformamide (DMF), dichloromethane (DCM), potassium hydroxide (KOH), sodium thiosulfate pentahydrate, and hydrochloric acid (HCl) were purchased from Fisher Scientific. Thionyl chloride (SOCl$_2$), 4-dimethylaminopyridine (DMAP), 2-nitroterephthalic acid, 4-hydroxybenzoic acid, metachloroperoxy-benzoic acid (MCPBA), (3-Aminopropyl) triethoxysilane (APTES), allyl alcohol and (±)-glycidol were purchased from Sigma Aldrich. 4-Cyano-4'-pentylbiphenyl (5CB) was purchased from Kingston Chemicals Limited. Polyimide (Durimide 32A) was purchased from Arch Chemicals. Liquid crystal monomers, 4-ethoxy-4'-(6-acryloyloxyhexyloxy) azobenzene (LCM_AZO), were kindly provided by the US Air Force Research Laboratory, and RM257 was obtained from Merck.

**Synthesis of Liquid Crystal Monomers (Chemical Structures in Fig. 2 and ^{1}H-NMR Spectra in *SI Appendix*, Fig. S2).**

*2-Nitro terephthaloyl dichloride(1).* A total of 4.22 g 2-nitroterephthalic acid (20 mmol) was mixed with 20 mL thionyl chloride under stirring. Two drops of DMF were added as catalyst. The mixture was heated to 75 °C and refluxed until no bubbles were generated from the solution. The reaction mixture was then cooled down to room temperature, and excess thionyl chloride was removed in vacuo. The crude 2-nitro terephthaloyl dichloride was obtained as an orange oil and used in the next step without further purification.

*2-Nitro, 1,4-benzenedicarboxylic acid, 1,4-bis(4-carboxyphenyl) ester(2).* A total of 3.45 g 4-hydroxybenzoic acid (25 mmol) was gradually dissolved into 2.8 g KOH (50 mmol) aqueous solution (100 mL), and the solution was cooled in an ice water bath. A total of 2.48 g of (*1*) (10 mmol) was dissolved in 15 mL ethyl acetate and added dropwise into the above prepared aqueous solution under vigorous stirring. After 30 min, the reaction was stopped and the mixture was neutralized by diluted HCl (5 vol%) aqueous solution to pH 7. The resulting precipitate was then filtered off by vacuum filtration and washed with ethanol to obtain 4.28 g of product (*2*) (9.5 mmol, 95% yield) as a white solid. ^{1}H-NMR (360 MHz, DMSO-d6): δ(ppm) = 7.41 (m, 4H, ArH of d), 8.02 (m, 4H, ArH of e), 8.36 (d, 1H, ArH of c), 8.65 (d, 1H, ArH of b), 8.79 (s, 1H, ArH of a).

*2-Nitro, 1,4-benzenedicarboxylic acid, 1,4-bis[4-(chlorocarbonyl)phenyl] ester(3).* A total of 4.06 g of (*2*) (9 mmol) was mixed with 15 mL thionyl chloride under stirring. Two drops of DMF were added as catalyst. The mixture was heated to 75 °C and refluxed until no bubbles were generated from the solution. The reaction mixture was then cooled down to room temperature, and the excess thionyl chloride was removed in vacuo. The crude product (*3*) was obtained as a white solid and used in the next step without further purification.

*2-Nitro, 1,4-benzenedicarboxylic acid, 1,4-bis[4-[(2-oxiranylmethoxy)carbonyl]phenyl] ester(4, LCM_X1).* A total of 1.3 g (±)-glycidol (17.6 mmol) and 3.90 g of (*3*) (8 mmol) were dissolved in 30 mL DCM, and the solution was cooled in an ice water bath at 0 °C. A total of 2.15 g DMAP (17.6 mmol) in 20 mL DCM was added dropwise into the above prepared solution under stirring. The reaction mixture was then gradually warmed up to room temperature and kept for another 6 h. The completion of the reaction was monitored with TLC until the reactant (*3*) was completely consumed. The mixture was then filtered through a celite pad, and the solvent was removed in vacuo. The resulting oil was purified by column chromatography (silica gel; eluent: DCM, followed by ethyl acetate: DCM = 1:15 vol/vol; R$_f$ ∼ 0.4) to obtain 3.06 g (*4*) (68% yield) as a white solid. ^{1}H-NMR (360 MHz, CDCl$_3$): δ(ppm) = 2.75 (dd, 2H, −(O)COCH$_2$CHCH$_2$O), 2.93 (dd, 2H, −(O)COCH$_2$CHCH$_2$O), 3.36 (m, 2H, −(O)COCH$_2$CHCH$_2$O), 4.20 (dd, 2H, −(O)COCH$_2$CHCH$_2$O), 4.71 (dd, 2H, −(O)COCH$_2$CHCH$_2$O), 7.38 (m, 4H, ArH of d), 8.04 (d, 1H, ArH of c), 8.20 (m, 4H, ArH of e), 8.59 (d, 1H, ArH of b), 8.88 (s, 1H, ArH of a).

*2-Nitro, 1,4-benzenedicarboxylic acid, 1,4-bis[4-[(2-propen-1-yloxy)carbonyl]phenyl] ester(5, LCM_X2).* A total of 1.02 g allyl alcohol (17.6 mmol) and 3.90 g of (*3*) (8 mmol) were dissolved in 30 mL DCM, and the solution was cooled in an ice water bath at 0 °C. A total of 2.15 g DMAP (17.6 mmol) in 20 mL DCM was added dropwise into the above prepared solution under stirring. The reaction mixture was then gradually warmed up to room temperature and kept for another 6 h. The completion of the reaction was monitored with TLC until the reactant (*3*) was completely consumed. The mixture was then filtered through a celite pad, and the solvent was removed in vacuo. The resulting oil was purified by column chromatography (silica gel; eluent: DCM, followed by ethyl acetate: DCM = 1:30 vol/vol) to obtain 2.83 g (*5*) (66.5% yield) as a white solid. ^{1}H-NMR (360MHz, CDCl$_3$): δ(ppm) = 4.87 (dd, 4H, −(O)COCH$_2$CHCH$_2$), 5.32 (d, 2H,



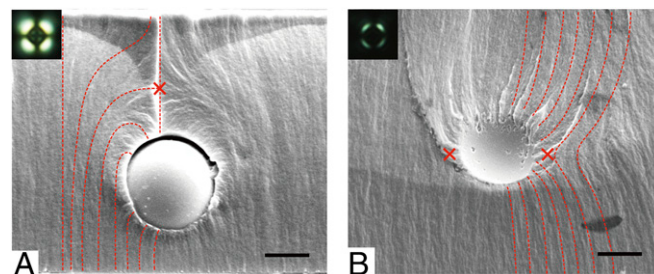**Fig. 5.** (*A* and *B*) SEM images of silica colloids suspended in LCP where either a point defect (*A*) or a line defect (*B*) was formed to screen the charge of the colloid. (*A* and *B*, *Insets*) POM images of point (*A*) and line (*B*) defects circumscribing silica colloids. The director field of the LC is represented by the red dotted line and the red crosses show the positions of defects. (Scale bars: 2 μm.)
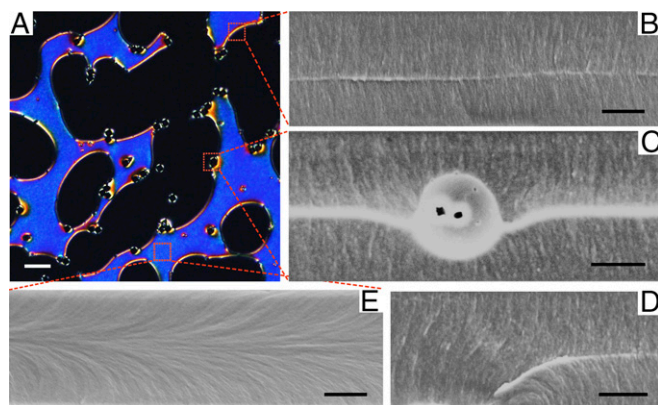
**Fig. 6.** Metastable configurations. (*A*) POM image of silica colloids suspended in LCM resulting in coexistence of homeotropic and planar-like regions, where the metastable planar regions (blue color) are stabilized by silica colloids. (*B*, *C*, and *E*) SEM images characterizing the local director field at different positions in *A* as indicated by the red dotted squares. (*B*) SEM image taken at the boundary between homeotropic and planar regions of LC, where a bright line in the middle of the image is shown, indicating the presence of a disclination line. (*C*) SEM image of a silica colloid sitting at the boundary. The bright line in the image shows a line defect in the bulk of LC that merged with the Saturn ring defect encircling the colloid. The silica colloid was trapped in the middle of the LC cell, and sank slightly downward. (*D*) SEM image of fiber-like structure that shows a bulk dis-clination line pinned to the bottom surface, as indicated by the bending white line. (*E*) SEM image of local LC director field inside an escaped region. Horizontally aligned fiber-like fractures indicating planar alignment of LC director field were found in the middle of the image, where the bending fiber-like fractures from top and bottom boundaries merged. (Scale bars: *A*, 20 μm; *B–E*, 3 μm.)

$-(O)COCH_2CHC\underline{H}_2$), 5.44 (d, 2H, $-(O)COCH_2CHC\underline{H}_2$), 6.06 (m, 2H, $-(O)COC\underline{H}_2CHCH_2$), 7.37 (m, 4H, ArH of d'), 8.04 (d, 1H, ArH of c'), 8.20 (m, 4H, ArH of e'), 8.60 (d, 1H, ArH of b'), 8.88 (s, 1H, ArH of a').

*4-(4-(((Oxiran-2-yl)methoxy)carbonyl)phenyl) 1-(4-((allyloxy)carbonyl)phenyl) 2-nitro-benzene -1,4-dioate (6, LCM_X3).* A total of 6.8 g (12.8 mmol) of (**5**) was dissolved in 30 mL DCM at 0 °C. A total of 3.31 g MCPBA (20 mmol) was gradually added to the solution. The reaction mixture was then warmed up to room temperature and allowed to stir for additional 48 h. After reaction, the white precipitate was filtered off and the resulting solution was washed twice with sodium thio-sulfate pentahydrate aqueous solution and then washed twice with brine. The solution was then dried with $MgSO_4$ and the solvent was removed in vacuo. The crude solid was purified by column chromatography (silica gel; eluent, DCM, followed by ethyl acetate: DCM = 1:30 vol/vol) to obtain 2.1g (**6**) (30% yield). $^1$H-NMR (360MHz, $CDCl_3$): δ(ppm) = 2.75 (dd, 1H, $-(O)COCH_2CHC\underline{H}_2O$), 2.93 (dd, 1H, $-(O)COCH_2CHC\underline{H}_2O$), 3.36 (m, 1H, $-(O)COCH_2C\underline{H}CH_2O$), 4.20 (dd, 1H, $-(O)COC\underline{H}_2CHCH_2O$), 4.71 (dd, 1H, $-(O)COC\underline{H}_2CHCH_2O$), 4.87 (dd, 2H, $-(O)COC\underline{H}_2CHCH_2$), 5.32 (d, 1H, $-(O)COCH_2CHC\underline{H}_2$), 5.44 (d, 1H, $-(O)COCH_2CHC\underline{H}_2$), 6.06 (m, 1H, $-(O)COC\underline{H}_2CHCH_2$),7.38 (m, 4H, ArH of d''), 8.04 (d, 1H, ArH of c''), 8.20 (m, 4H, ArH of e''), 8.59 (d, 1H, ArH of b''), 8.88 (s, 1H, ArH of a'').

**Preparation of Liquid Crystal Monomer Solutions.** A total of 200 mg liquid crystal monomer (**4**, LCM_X1) and 4 mg Iragcure 261 (2 wt%; Ciba Specialty Chemicals) as photoacid generator (PAG) were dissolved in 10 g DCM and kept in a cool and dark place before use.

**Fabrication of Patterned Substrates.** All of the patterned substrates were fabricated by replica molding from commercially available epoxy (D.E.R. 354; Dow Chemical) on glass slides, using poly(dimethylsiloxane) (PDMS) molds, following the procedure reported in the literature (50).
*Preparation of substrates with desired LC anchoring.*

i) Homeotropic anchoring of LCs on flat substrates, porous membranes, and square channels. The anchoring type of the LC (homeotropic or planar) largely depends on the surface energy of the interface (51). For many types of LCMs, hydrophilic surfaces with high surface energy usually give homeotropic anchoring. In our system, all liquid crystal monomers, LCM_X1, LCM_X2, and LCM_X3, were found to have homeotropic anchoring on a $SiO_2$ surface. Here, we used precleaned glass slides as the flat substrates or coated patterned polymer substrates with a thin layer of $SiO_2$ through a chemical vapor deposition

(CVD) process according to the literature (52). In brief, patterned sub-strates kept in a desiccator under vacuum were first exposed to chem-ical vapors of silicon tetrachloride ($SiCl_4$, 0.2 mL) for 10–15 min. Then the samples were exposed to a humidity chamber (humidity ~90%) for 10 min, followed by immersion in a pyridine aqueous solution (3 vol%) for 5–10 min. The final substrates were obtained by washing with ethanol and deionized (DI) water, respectively, three times, followed by drying by an air gun and baking at 100 °C in a convection oven for 15 min to 1 h.

ii) Strong homeotropic anchoring of LCM_X1 on micropillar arrays. To achieve high homeotropic anchoring energy on micropillar arrays, we first treated pillars based on step (*i*), followed by functionalization of the $SiO_2$ surface with APTES. Due to the Michael-addition reactions between the amino groups in APTES and epoxy groups in LCM_X1, the newly formed surface anchored LCM_X1, where the mesogenic groups were orientated perpendicularly to the interface. As a result, the interaction between the interface and LCM molecules was substan-tially increased, showing stronger homeotropic anchoring than the $SiO_2$-coated surface. In detail, the sample consisting of the micropillar array was immersed in a solution of 1 vol% APTES in an ethanol/water mixture (90:10 vol/vol) for ~10 min and then rinsed with ethanol and DI water three times and dried by air gun. Finally, the sample was baked in a convection oven at 100 °C for 15 min to 1 h.

iii) Planar anchoring. To create planar anchoring for LCMs, a glass substrate was spin coated with a thin layer of polyimide from its xylene solution at 5,000 rpm (on spin coater WS-650Hzb-23NPP-UD-3; Laurell) for 30 s, followed by baking at 130 °C for 20 min. A uniform planar anchoring sample was obtained by rubbing the polyimide-coated substrate with a velvet cloth.

*Liquid crystal cell preparation.*

i) On patterned substrates. Approximately 20–40 μL LCM_X1/DCM solution was placed on the patterned substrate, and solvent DCM was evaporated at 130 °C for at least 10 min. Then the LCM_X1 liquid was sandwiched between the substrate and another cover glass (treat if needed) at 130 °C. The sample was then cooled down to the desired temperature (cooling rate not critical here) to align LC.

ii) With silica colloids. Five-micrometer diameter silica colloids (Sigma Aldrich) were dispersed in a LCM_X1/DCM solution (note that a high concentration of ~20 wt% was preferred), and the mixture was sonicated for at least 15 min to obtain a homogeneous suspension. To prepare the LC cell with silica colloids, several drops (~20–40 μL) of the suspension were placed on a clean glass slide, and the solvent was evaporated at 130 °C for at least 10 min. Then another precleaned glass slide was placed on top to make a LC cell. The thickness of the LC cell was roughly controlled as ~10 μm. The sample was then cooled down from 130 °C to the desired temperature (cooling rate not critical here) to align the LC.

**UV Cross-Linking.** To prevent the reorientation of the directors of LCM_X1 during photopolymerization, UV curing was carefully performed in three steps, including (*i*) samples were slowly cooled down at 1 °C/min to room tem-perature (~25 °C); (*ii*) samples were exposed to a low UV power (~2 mW/cm$^2$ at 365 nm, Hg lamp), overnight; and (*iii*) after UV exposure, samples were slowly heated up to 100 °C at a ramping rate of 1 °C/min on a Mettler FP82 and FP90 thermo-system hot stage in ambient air, followed by baking at 120 °C for another 1–2 h to completely cure the epoxy groups.

**Characterization.** Chemical structures of the synthesized chemicals were confirmed with $^1$H-NMR performed on a Bruker Advance DMX 360 (360 MHz) spectrometer at 25 °C and analyzed with TOPSPIN software. Thermo analysis of the synthesized LCMs was performed on a differential scanning calorimetry (DSC) Q2000 (TA Instruments). Samples were heated and cooled under nitrogen with a ramping rate of 10 °C/min for three cycles. Data from the second cycle were reported. Liquid crystal phases and alignments were observed under an Olympus BX61 motorized optical microscope with crossed polarizers, using CellSens software. Liquid crystal polymer samples were manually broken into pieces or cut with a razor blade. The cross-section was coated with a 4-nm iridium layer for SEM. Imaging was performed on a dual-beam FEI Strata DB 235 Focused Ion Beam (FIB)/SEM instrument with a 5-kV electron beam.

**Measurement of Refractive Index and Birefringence.** We used Snell's law to estimate the refractive indexes of LCM_X1 by comparing the apparent thick-ness of the LC cell, $D_{LC}$, with the actual cell thickness without LC, $D_0$; that is,

$n_{e,o} = D_0/D_{LC}$. We prepared a uniform planar cell in the way same as described earlier. $D_0$ and $D_{LC}$ were measured before and after LC was infiltrated, respectively. Accordingly, we obtained the extraordinary refractive index, $n_e$ ~1.67 ± 0.02 and the ordinary refractive index, $n_o$ ~ 1.5 ± 0.02 of LC when the polarized light was parallel and perpendicular to the LC director, respectively. The birefringence of LCM_X1 was estimated as ~0.17. We also estimated birefringence of LCM_X1 from a wedge cell, using the Michael–Levy chart before and after UV curing, as 0.16 ± 0.02, in good agreement with that measured from optical microscopy. Again, the consistent birefringence before and after polymerization as shown in Fig. 3 D and E clearly indicates that polymerization did not affect the nematic order parameter.

1. Higgins DA, Luther BJ (2003) Watching molecules reorient in liquid crystal droplets with multiphoton-excited fluorescence microscopy. *J Chem Phys* 119(7):3935–3942.
2. Kachynski AV, Kuzmin AN, Prasad PN, Smalyukh II (2007) Coherent anti-Stokes Raman scattering polarized microscopy of three-dimensional director structures in liquid crystals. *Appl Phys Lett* 91(15):151905.
3. Smalyukh II, Shiyanovskii SV, Lavrentovich OD (2001) Three-dimensional imaging of orientational order by fluorescence confocal polarizing microscopy. *Chem Phys Lett* 336(1–2):88–96.
4. Feller MB, Chen W, Shen YR (1991) Investigation of surface-induced alignment of liquid-crystal molecules by optical second-harmonic generation. *Phys Rev A* 43(12):6778–6792.
5. Yelin D, Silberberg Y, Barad Y, Patel JS (1999) Phase-matched third-harmonic generation in a nematic liquid crystal cell. *Phys Rev Lett* 82(15):3046–3049.
6. Yoon DK, et al. (2007) Internal structure visualization and lithographic use of periodic toroidal holes in liquid crystals. *Nat Mater* 6(11):866–870.
7. Zhang C, et al. (2012) Direct observation of smectic layers in thermotropic liquid crystals. *Phys Rev Lett* 109(10):107802.
8. Gao M, et al. (2014) Direct observation of liquid crystals using cryo-TEM: Specimen preparation and low-dose imaging. *Microsc Res Tech* 77(10):754–772.
9. Yoon DK, et al. (2013) Three-dimensional textures and defects of soft material layering revealed by thermal sublimation. *Proc Natl Acad Sci USA* 110(48):19263–19267.
10. Costello MJ, Meiboom S, Sammon M (1984) Electron microscopy of a cholesteric liquid crystal and its blue phase. *Phys Rev A* 29(5):2957–2959.
11. Livolant F, Bouligand Y (1989) Freeze-fractures in cholesteric mesophases of polymers. *Mol Cryst Liq Cryst* 166(1):91–100.
12. Bouligand Y (1972) Twisted fibrous arrangements in biological materials and cholesteric mesophases. *Tissue Cell* 4(2):189–217.
13. Donald AM, Viney C, Windle AH (1983) Banded structures in oriented thermotropic polymers. *Polymer* 24(2):155–159.
14. Mitchell GR, Windle AH (1982) Structural analysis of an oriented liquid crystalline copolyester. *Polymer* 23(9):1269–1272.
15. Cavallaro M, Jr, et al. (2013) Exploiting imperfections in the bulk to direct assembly of surface colloids. *Proc Natl Acad Sci USA* 110(47):18804–18808.
16. Bishop DJ, Gammel PL, Huse DA, Murray CA (1992) Magnetic flux-line lattices and vortices in the copper oxide superconductors. *Science* 255(5041):165–172.
17. Tchernyshyov O, Chern G-W (2005) Fractional vortices and composite domain walls in flat nanomagnets. *Phys Rev Lett* 95(19):197204.
18. Kibble TWB (1976) Topology of cosmic domains and strings. *J Phys Math Gen* 9(8):1387.
19. Nikkhou M, et al. (2015) Light-controlled topological charge in a nematic liquid crystal. *Nat Phys* 11(2):183–187.
20. Modes CD, Bhattacharya K, Warner M (2010) Disclination-mediated thermo-optical response in nematic glass sheets. *Phys Rev E Stat Nonlin Soft Matter Phys* 81(6 Pt 1):060701.
21. Ware TH, McConney ME, Wie JJ, Tondiglia VP, White TJ (2015) Actuating materials. Voxelated liquid crystal elastomers. *Science* 347(6225):982–984.
22. Dierking I (2010) Recent developments in polymer stabilised liquid crystals. *Polym Chem* 1(8):1153–1159.
23. Dierking I, Archer P (2013) Imaging liquid crystal defects. *RSC Advances* 3(48):26433–26437.
24. Broer DJ, Bastiaansen CMW, Debije MG, Schenning APHJ (2012) Functional organic materials based on polymerized liquid-crystal monomers: Supramolecular hydrogen-bonded systems. *Angew Chem Int Ed Engl* 51(29):7102–7109.
25. Küpfer J, Finkelmann H (1991) Nematic liquid single crystal elastomers. *Makromol Chem Rapid Commun* 12(12):717–726.
26. Ohm C, Brehmer M, Zentel R (2010) Liquid crystalline elastomers as actuators and sensors. *Adv Mater* 22(31):3366–3387.
27. Thomsen DL, et al. (2001) Liquid crystal elastomers with mechanical properties of a muscle. *Macromolecules* 34(17):5868–5875.
28. Yu Y, Nakano M, Ikeda T (2003) Photomechanics: Directed bending of a polymer film by light. *Nature* 425(6954):145–145.
29. Warner M, Terentjev EM (2003) *Liquid Crystal Elastomers* (Clarendon, Oxford).
30. Broer DJ, Crawford GP, Zumer S (2011) *Cross-Linked Liquid Crystalline Systems: From Rigid Polymer Networks to Elastomers* (CRC, New York).
31. Petrov VF, Shimizu Y (2001) Nitro substitution in achiral calamitic liquid crystals. *Liq Cryst* 28(11):1627–1647.
32. Dewar MJS, Goldberg RS (1970) Effects of central and terminal groups on nematic mesophase stability. *J Org Chem* 35(8):2711–2715.
33. Lee JY, Jang J, Hong SM, Hwang SS, Kim KU (1999) Relationship between the structure of the bridging group and curing of liquid crystalline epoxy resins. *Polymer* 40(11):3197–3202.
34. Minkin VI, Osipov OA, Zhdanov YA (1970) *Dipole Moments in Organic Chemistry* (Plenum, New York).
35. Zuev VV, de Vekki DA (2006) Catalytic isomerization of terminal olefins in liquid-crystalline polyesters at hydrosilylation with 1-(1′-arylethoxy)-1,1,3,3-tetramethyldisiloxanes. *Russ J Org Chem* 42(8):1105–1112.
36. Faetti S (1998) The effects of curvature on nematic liquid crystals confined in a cylindrical cavity. *Phys Lett A* 237(4–5):264–270.
37. Crawford GP, Allender DW, Doane JW (1992) Surface elastic and molecular-anchoring properties of nematic liquid crystals confined to cylindrical cavities. *Phys Rev A* 45(12):8693–8708.
38. Shaw JM, Gelorme JD, LaBianca NC, Conley WE, Holmes SJ (1997) Negative photoresists for optical lithography. *IBM J Res Dev* 41(1.2):81–94.
39. Ito H (1997) Chemical amplification resists: History and development within IBM. *IBM J Res Develop* 41(1–2):69–80.
40. Broer DJ, Lub J, Mol GN (1993) Synthesis and photopolymerization of a liquid-crystalline diepoxide. *Macromolecules* 26(6):1244–1247.
41. Jahromi S, Lub J, Mol GN (1994) Synthesis and photoinitiated polymerization of liquid crystalline diepoxides. *Polymer* 35(3):622–629.
42. van Oosten CL, Bastiaansen CWM, Broer DJ (2009) Printed artificial cilia from liquid-crystal network actuators modularly driven by light. *Nat Mater* 8(8):677–682.
43. Berreman DW, Meiboom S, Zasadzinski JA, Sammon MJ (1986) Theory and simulation of freeze-fracture in cholesteric liquid crystals. *Phys Rev Lett* 57(14):1737–1740.
44. Zasadzinski JA, Bailey SM (1989) Applications of freeze-fracture replication to problems in materials and colloid science. *J Electron Microsc Tech* 13(4):309–334.
45. Hudson SD, Thomas EL (1989) Frank elastic-constant anisotropy measured from transmission-electron-microscope images of disclinations. *Phys Rev Lett* 62(17):1993–1996.
46. Lapointe CP, Mason TG, Smalyukh II (2009) Shape-controlled colloidal interactions in nematic liquid crystals. *Science* 326(5956):1083–1086.
47. Senyuk B, et al. (2013) Topological colloids. *Nature* 493(7431):200–205.
48. Poulin P, Stark H, Lubensky TC, Weitz DA (1997) Novel colloidal interactions in anisotropic fluids. *Science* 275(5307):1770–1773.
49. Muševič I, Škarabot M, Tkalec U, Ravnik M, Žumer S (2006) Two-dimensional nematic colloidal crystals self-assembled by topological defects. *Science* 313(5789):954–958.
50. Zhang Y, Lo C-W, Taylor JA, Yang S (2006) Replica molding of high-aspect-ratio polymeric nanopillar arrays with high fidelity. *Langmuir* 22(20):8595–8601.
51. Warenghem M (1982) A test for surface energy anisotropy sign determination. *Mol Cryst Liq Cryst* 89(1–4):15–21.
52. Klaus JW, George SM (2000) SiO2 chemical vapor deposition at room temperature using SiCl4 and H2O with an NH3 catalyst. *J Electrochem Soc* 47(7):2658–2664.

Xia et al.